





Revealing ultrafast domain wall motion in Mn_2Au through permalloy capping

Sarah Jenkins ¹, Tobias Wagner ^{2,*}, Olena Gomonay ², and Karin Everschor-Sitte ¹

¹*Faculty of Physics and Center for Nanointegration Duisburg-Essen (CENIDE), University of Duisburg-Essen, 47057 Duisburg, Germany*

²*Institute of Physics, Johannes Gutenberg University Mainz, 55128 Mainz, Germany*



(Received 9 November 2023; revised 28 May 2024; accepted 10 June 2024; published 27 June 2024)

Antiferromagnets offer much faster dynamics compared to their ferromagnetic counterparts but their order parameter is extremely difficult to detect and control. So far, controlling the Néel order parameter electrically is limited to only very few materials where Néel spin-orbit torques are allowed by symmetry. In this work, we show that coupling a thin ferromagnet (permalloy) layer on top of an antiferromagnet (Mn_2Au) solves a major roadblock—the controlled reading, writing, and manipulation of antiferromagnetic domains. We confirm by atomistic spin dynamics simulations that the domain wall patterns in the Mn_2Au are imprinted on the permalloy, therefore allowing for indirect imaging of the Néel order parameter. Our simulations show that the coupled domain wall structures in Mn_2Au -Py bilayers can be manipulated by either acting on the Néel order parameter via Néel spin-orbit torques or by acting on the magnetization (the ferromagnetic order parameter) via magnetic fields. In both cases, we predict ultrahigh domain wall speeds on the order of 8.5 km/s. Thus, employing a thin ferromagnetic layer has the potential to easily control the Néel order parameter in antiferromagnets even where Néel spin-orbit torques are forbidden by symmetry. The controlled manipulation of the antiferromagnetic order parameter provides a promising basis for the development of high-density storage and efficient computing technologies working in the THz regime.

DOI: [10.1103/PhysRevB.109.224431](https://doi.org/10.1103/PhysRevB.109.224431)

I. INTRODUCTION

Spintronics has revolutionized data storage technology with spin current-based technologies such as hard disk drives. However, these devices are reaching the limit of possible technological advances in speed and size due to the intrinsic limits of ferromagnetic (FM) materials. In these devices, antiferromagnetic (AFM) materials are typically only used to provide a preferred direction of magnetization for the active FM components. Using AFMs instead of FMs as the active component could solve this problem due to their ultrafast dynamics, lack of external magnetic fields, and temperature stability of the Néel ordered state [1–7]. This brings massive advancements toward ultrafast and ultra-high-density spintronics.

One of the most promising materials for AFM spintronic-based devices is Mn_2Au due to its high Néel temperature, moderate anisotropy, and layered two-sublattice spin structure. It has been predicted that in certain AFMs, current-induced spin-orbit-torques (SOTs) can switch the sublattice magnetic orientation [1,2]. Recently these so-called Néel SOTs have been demonstrated experimentally for CuMnAs [8–11] and Mn_2Au [12–14], and materials with similar AFM ordering [15–18]. However, detecting the AFM magnetic signal is far more difficult due to the absence of a net magnetization.

Recently, a strong exchange coupling between Mn_2Au and thin layers of permalloy ($\text{Ni}_{80}\text{Fe}_{20}$) has been observed

[19,20]. As a consequence, the FM domain structure exactly maps the AFM domain structure [4,19]. Notably, the coercive field of Mn_2Au -Py is an order of magnitude higher (5000 Oe [19]) compared to other materials such as CuMnAs (~ 200 Oe [21]). High coercive fields lead to long-term stability at room temperature.

Due to the strong coupling, it is anticipated, that the AFM Néel vector and the FM magnetization rotate coherently when an external field is applied to the FM. While experimentally the ultrafast dynamics (\propto THz) and current induced Néel SOT switching have yet to be demonstrated in Mn_2Au -Py, this report aims to showcase the promising prospects of Mn_2Au -Py bilayers. Atomistic simulations are used to accurately resemble realistic crystal structures and material parameters in dynamics simulations. We derive a phenomenological model which is in agreement with the simulation results. Besides single domain states of the Mn_2Au -Py bilayer system, we simulate the driven dynamics of a domain wall percolating the FM-AFM bilayer by an applied magnetic field and Néel SOTs. In both cases, we observe a strongly coupled domain wall motion with domain wall speeds on the order of 8.5 km/s.

II. MODEL OF Mn_2Au -Py BILAYERS

Here, we model a Mn_2Au -Py bilayer system containing a 90-degree domain wall along the [100] direction which is capped by a thin layer of Py. The domain wall from the Mn_2Au permeates through to the permalloy due to the strong interface coupling as shown in Fig. 1(a). The crystal structures of permalloy and Mn_2Au are shown in Figs. 1(b) and 1(c), respectively. Although Py is amorphous in bulk, due to

*Contact author: tobias.wagner@uni-mainz.de

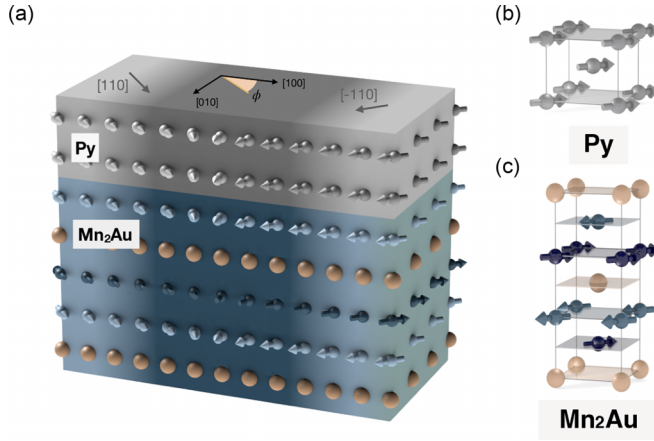


FIG. 1. (a) Schematic diagram of a 90-degree magnetic domain wall in a Mn_2Au -Py bilayer. The Mn_2Au layer is shown in blue and is capped by permalloy shown in gray. (b) and (c) detail the magnetic structures of permalloy and Mn_2Au , respectively.

interface lattice matching with the Mn_2Au we presume that Py will have a BCC structure in the interface region of the thin films we are simulating. The lattice structure of Mn_2Au has two AFM coupled planes of Mn atoms and a plane of gold atoms. The Hamiltonian \mathcal{H} of the Mn_2Au -Py bilayer is comprised of three contributions

$$\mathcal{H} = \mathcal{H}_{\text{Mn}_2\text{Au}} + \mathcal{H}_{\text{Py}} + \mathcal{H}_{\text{int}} : \quad (1)$$

the Hamiltonian describing Mn_2Au ($\mathcal{H}_{\text{Mn}_2\text{Au}}$), the Hamiltonian for permalloy (\mathcal{H}_{Py}), and the Hamiltonian for the interface (\mathcal{H}_{int}).

The Hamiltonian for Mn_2Au up to the fourth order in anisotropy is given by [22]

$$\begin{aligned} \mathcal{H}_{\text{Mn}_2\text{Au}} = & - \sum_{i<j} (\mathbf{S}_i \mathbf{J}_{ij}^{\text{Mn}_2\text{Au}} \mathbf{S}_j + S_i^z \tilde{\mathbf{J}}_{ij}^{\text{Mn}_2\text{Au}} S_j^z) \\ & + \sum_i (k_4 (S_i^z)^4 + k_\phi (S_i^x)^2 (S_i^y)^2) + \mathcal{H}_d, \quad (2) \end{aligned}$$

where $\mathbf{S}_{i,j}$ are unit vectors describing the local spin directions on sites i, j . The first term describes the exchange energy, which incorporates the second order two-ion anisotropy [23]. The second term describes the anisotropy, and \mathcal{H}_d represents the magnetostatic fields, which are calculated using an effective macrocell approach [24]. The dominant anisotropy in Mn_2Au is the out-of-plane anisotropy $k_4 < 0$ that creates an easy plane. The weaker in-plane anisotropy breaks the in-plane rotational symmetry favoring the four symmetry equivalent $\langle 110 \rangle$ directions, i.e., $k_\phi > 0$ [22]. For the atomistic spin dynamics, we take three nearest neighbors into account: the first and second nearest neighbor interactions are ferromagnetic and exist between atoms in the same Mn sublattice. The third nearest neighbor interaction is antiferromagnetic between Mn atoms in different sublattices, see Appendix A for details.

The Hamiltonian for Py is given by

$$\mathcal{H}_{\text{Py}} = - \sum_{i<j} \mathbf{S}_i \mathbf{J}_{ij}^{\text{Py}} \mathbf{S}_j + \frac{k_c^{\text{Py}}}{2} \sum_i (S_x^4 + S_y^4 + S_z^4) + \mathcal{H}_d. \quad (3)$$

The first term describes the exchange energy of the permalloy, and the second term is a weak cubic anisotropy.

The interface Hamiltonian

$$\mathcal{H}_{\text{int}} = - \sum_{i<j} \mathbf{S}_i \mathbf{J}_{ij}^{\text{int}} \mathbf{S}_j + \mathcal{H}_d \quad (4)$$

acts between the manganese and the permalloy atoms. It leads to a strong coupling between the two layers and imprints the magnetic structures of Mn_2Au in permalloy. For permalloy [25] as well as for the interface we use a Heisenberg exchange with a nearest neighbor approximation in the atomistic spin dynamics simulations. In Appendix A we list the parameters used for the simulations.

For investigations with an external field \mathbf{B}_{ext} , we add

$$\mathcal{H}_{\text{ext}} = - \sum_i \mu_s \mathbf{S}_i \cdot \mathbf{B}_{\text{ext}} \quad (5)$$

to the Hamiltonian \mathcal{H} in Eq. (1). Note that the external magnetic field is applied to every spin in the system where μ_s refers to the spin moment in the respective layer (μ_{Py} and μ_{Mn} are given in Table I in Appendix A). As AFMs are largely impervious to magnetic fields, the applied field mostly affects the permalloy. However, due to the strong exchange coupling between the FM and the AFM, the magnetic order in Mn_2Au is indirectly affected by an applied field as well.

III. STATIC PROPERTIES OF SINGLE DOMAIN STATES IN THE BILAYER SYSTEM

We performed Monte Carlo simulations on the pure Mn_2Au system (for a system size of $8 \text{ nm} \times 8 \text{ nm} \times 5 \text{ nm}$) which reproduced the low-temperature ground state spin structure with the magnetization of the two Mn sublattices 180 degrees apart, see Fig. 1(c). The easy axes are along the $\langle 110 \rangle$ direction, in agreement with previous neutron scattering experiments [26] and theoretical calculations [22,27]. Because of the high Néel temperature of Mn_2Au , the magnetic state is largely independent from thermal effects at room temperature.

For the bilayer system (of lateral size $8 \text{ nm} \times 8 \text{ nm}$, and thickness 5 nm of Mn_2Au and 1 nm of permalloy) we find that the ground state of Mn_2Au is imprinted into the Py due to the strong interface exchange coupling [19]. Performing constrained Monte Carlo simulations [28], we computed the energy surfaces for a single domain state in the bilayer system [29]. When a magnetic field is applied, the fourfold degeneracy in the energy surface is broken. The applied magnetic field was along the [110] direction, and the energy surface, therefore, favors this easy axis over the other three easy axis directions. To characterize the in-plane spin direction, we introduce the angle ϕ as the angle from the [100] axis in the xy plane, see Fig. 1. By scanning all angles ϕ we obtain the energy surfaces for varying field strengths as shown in Fig. 2. The field direction, i.e., $\phi = \pi/4$, is energetically

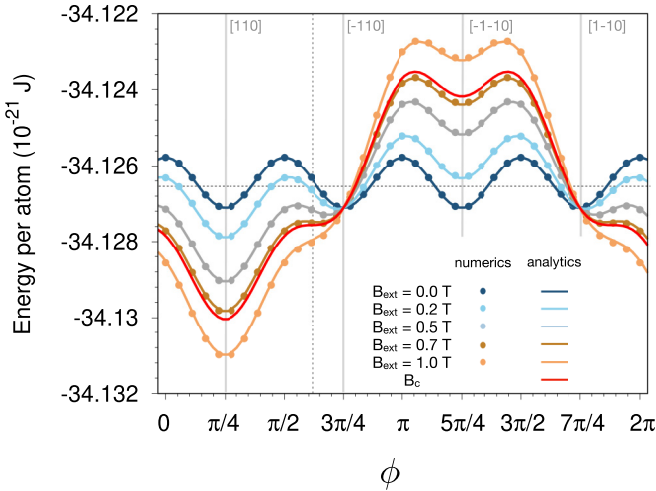


FIG. 2. Energy surfaces of a Mn₂Au-Py bilayer (average energy per atom) with an applied field of varying strength along the [110] direction, with the critical field $B_c \approx 0.7555$ T. The Mn₂Au thickness was 5 nm and the permalloy thickness was 1 nm.

preferred. For magnetic domains oriented perpendicular to the field direction, i.e., $\phi = 3\pi/4$ and $\phi = 7\pi/4$, the energy of the system is independent of the strength of the magnetic field. The easy axis direction which is antiparallel to the magnetic field, i.e., $\phi = 5\pi/4$, gets enhanced in energy with increasing field strength. A spherical version of Fig. 2 can be found in Appendix B.

The strong in-plane anisotropy of Mn₂Au and the strong interface coupling causes the spins in the two layers to be effectively in plane. For a single domain state with an applied magnetic field along the [110] direction (as shown in Fig. 2), the system can be described by an effective Hamiltonian $\mathcal{H}_{\text{bilayer}}$ described by the angle ϕ ,

$$\mathcal{H}_{\text{bilayer}}(\phi) = E_0 + c_\phi k_\phi \cos 4\phi - c_B \mu_{\text{Py}} B_{\text{ext}} \cos(\phi - \pi/4). \quad (6)$$

Here E_0 is the energy of the system without the fourfold in-plane anisotropy term. The magnetic field couples to the magnetization, i.e., the average spin moment of permalloy per atom μ_{Py} , in the form of a $\cos \phi + \sin \phi$ term which can be rewritten as a shifted cosine function, as $\cos \phi + \sin \phi = \sqrt{2} \cos(\phi - \pi/4)$. The constants c_ϕ and c_B depend on the system. c_ϕ is proportional to the layer thickness of the Mn₂Au, whereas c_B is proportional to the layer thickness of the permalloy.

Upon increasing the magnetic field strength above a critical field value B_c , the metastable states (previously oriented approximately perpendicular to the applied field) disappear. At the critical field value B_c , the local minima close to $\phi = 3\pi/4$ and $7\pi/4$ turn into saddle points, with (i) $\partial \mathcal{H}_{\text{bilayer}}(\phi)/\partial \phi|_{\phi=\tilde{\phi}} = 0$, (ii) $\partial^2 \mathcal{H}_{\text{bilayer}}(\phi)/\partial \phi^2|_{\phi=\tilde{\phi}} = 0$, and (iii) $\partial^3 \mathcal{H}_{\text{bilayer}}(\phi)/\partial \phi^3|_{\phi=\tilde{\phi}} \neq 0$. Solving these three equations close to $\phi = 3\pi/4$, we obtain

$$B_c = \frac{16\sqrt{6}k_\phi c_\phi}{9\mu_{\text{Py}} c_B} \quad (7)$$

with $\tilde{\phi} = 3\pi/4 - \delta\phi \approx 1.9357$ being independent of the model parameters. Using the parameters summarized in Appendix A we obtain from the simulation results $E_0 \approx -34.1264 \cdot 10^{-21}$ J/atom, $c_\phi = 0.8375$, and $c_B = 0.2603$. For the critical field value, we obtain $B_c \approx 0.7555$ T.

IV. DOMAIN WALLS IN Mn₂Au-Py BILAYER SYSTEMS

In this section, we study a static domain wall across a ribbon bilayer system of dimensions 1000 nm along x and 40 nm along y . The z height of Mn₂Au is kept constant at 5 nm, the Py height is initially 1 nm, but this is later varied. A 90-degree domain wall from the [110] direction to the [1-10] direction was initialized at $x = 100$ nm in both the Mn₂Au and the Py, see Figs. 1 and 3(a). Our key findings are summarized below: (i) The domain wall of Mn₂Au is imprinted on the permalloy capping. (ii) The bilayer structure has a net remaining magnetization from the permalloy which then allows the observation of domain walls in the AFM via the capping [19]. (iii) The permalloy capping increases the average domain wall width of the bilayer system compared to pure Mn₂Au. (iv) The domain wall width varies along the vertical direction, with increasing domain wall width toward the top (i.e., FM) surface.

We computed the domain wall profile of the bilayer using a Monte Carlo integrator. The simulation was run for one million Monte Carlo steps at 0 K until the magnetic structure remained stationary. To characterize the domain wall, we then computed the sublattice magnetization by averaging over the atomic spins along z for each sublattice. For a macroscopic description we associate this vector with the Néel order parameter \mathbf{n} ($|\mathbf{n}| = 1$). Figure 3 (a) shows the normalized (height averaged) x component of the magnetic order parameter along the ribbon for the bilayer system and a comparison to pure Mn₂Au. The domain wall width was extracted by fitting the x component, $n_x = \cos \Theta(x)$, to the expression of the profile function

$$\Theta(x) = \arctan \left[\exp \left(\frac{x - x_0}{\delta_{\text{dw}}} \right) \right] + \frac{\pi}{4}. \quad (8)$$

Here x_0 is the position of the domain wall, and δ_{dw} the domain wall width. For the 90-degree domain wall, n_x varies from $n_x = 1/\sqrt{2}$ on the left, over to $n_x = 0$ in the center of the domain wall to $n_x = -1/\sqrt{2}$ on the right end, as shown in Figs. 3(a) and 3(b).

Our numerical results reveal a domain wall width of $\delta_{\text{dw}} \approx 29.3$ nm for the case of pure Mn₂Au. As the natural domain wall width of permalloy is about an order of magnitude larger, the average domain wall width of the bilayer system depends on the relative thickness of the permalloy to Mn₂Au. For 1 nm permalloy on top of 5 nm Mn₂Au, see Fig. 3, we obtain a domain wall width of $\delta_{\text{dw}} \approx 38.2$ nm, i.e., an increase of about 30%. For such a thin permalloy capping we do not observe a significant change of the domain wall width along the z direction.

Figure 3(c) displays the change of the domain wall width with height (z direction) for the device for varying capping layer thicknesses of permalloy. We find that the domain wall becomes wider toward the FM and there is a larger domain wall width change for thicker permalloy capping. The change in the domain wall width comes from the competition

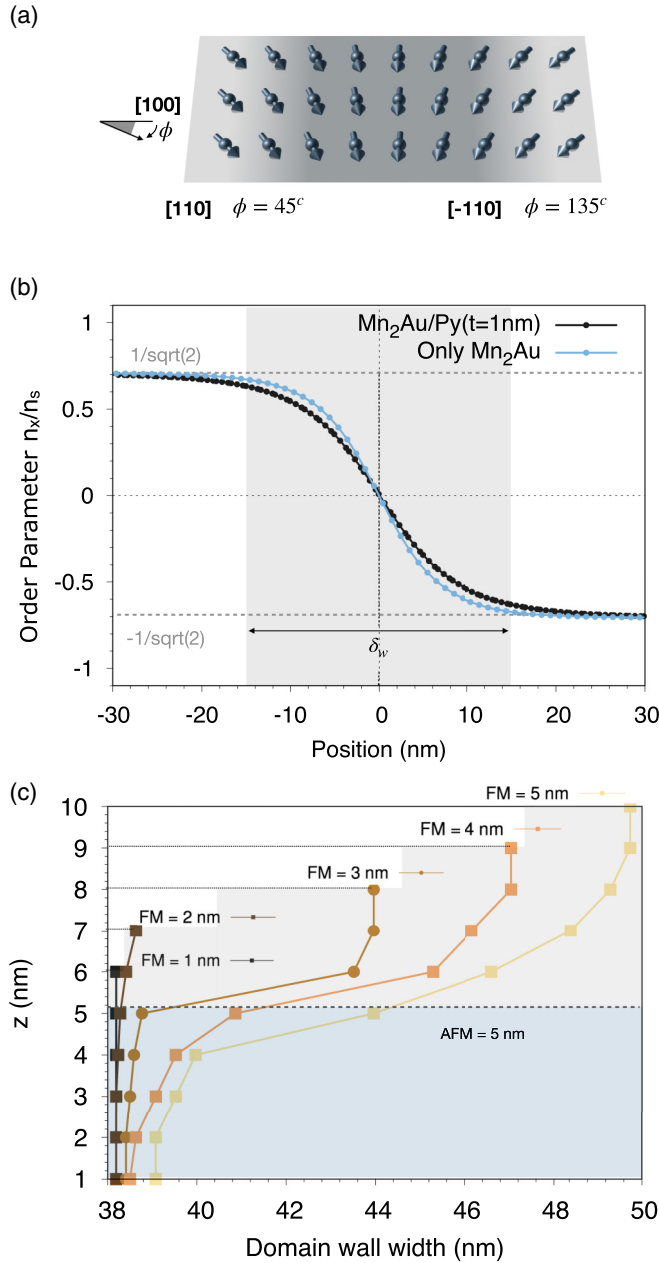


FIG. 3. Static domain wall structures in Mn₂Au-Py bilayers. (a) Sketch of a 90-degree domain wall. (b) Domain wall profiles n_x for a 5 nm thick Mn₂Au layer with a 1 nm permalloy capping and without permalloy capping. (c) Domain wall widths along the z direction for varying permalloy capping layer thicknesses.

between the magnetocrystalline anisotropy and the exchange interactions. The strength of the exchange interactions and anisotropy vary from bulk Mn₂Au to bulk Py across the interface, such that the domain wall widths vary. For thin Py capping layers the domain wall width in the Py matches the Mn₂Au due to the strong interface exchange coupling.

V. MANIPULATING DOMAIN WALLS IN Mn₂Au-Py BILAYER SYSTEMS

In this section, we focus on the dynamics of the previously considered domain walls in Mn₂Au-Py bilayer systems. Two

external driving mechanisms to move the domain wall are investigated separately: an external magnetic field and a current, which induces Néel SOTs. We disregard effects of thermal noise. Despite recent experiments in pure Mn₂Au showing that thermal noise plays an important role [13,14], in hybrid systems [19,20], the interface exchange coupling appears to be the most dominant effect.

The system dynamics were calculated by solving the stochastic Landau-Lifshitz-Gilbert equation [30]

$$\frac{\partial \mathbf{S}_i}{\partial t} = -\frac{\gamma_e}{1 + \lambda^2} [\mathbf{S}_i \times \mathbf{B}_{\text{eff}} + \lambda \mathbf{S}_i \times (\mathbf{S}_i \times \mathbf{B}_{\text{eff}})], \quad (9)$$

which models the interaction of an atomic spin moment \mathbf{S}_i with an effective field $\mathbf{B}_{\text{eff}} = -\delta \mathcal{H} / \delta \mathbf{S}_i$. The atomic moments precess around the effective field, where the frequency of precession is determined by the gyromagnetic ratio of an electron ($\gamma_e = 1.76 \cdot 10^{11} \text{ rad s}^{-1} \text{ T}^{-1}$). The damping constant λ is defined in each of the two materials, see Table I in Appendix A. For our numerical results, Eq. (9) was solved using a Heun scheme [24].

In the following, we considered a 1 nm permalloy capping on top of 5 nm Mn₂Au. The lateral dimensions of our system remain the same as in Sec. IV, i.e., 1000 nm along x , 40 nm along y . Our starting point is a relaxed 90-degree domain wall in the bilayer system from the [110] direction to the [1-10] located at $x = 100$ nm.

A. Magnetic field-driven domain wall dynamics

To study the magnetic field-driven domain wall dynamics, we apply a magnetic field along the [110] direction, making this direction the energetically preferred one. To reduce the energy of the bilayer system, the [110] domain in the permalloy is shifted via a domain wall motion. Due to the strong interface exchange coupling between the two layers, the domain wall in the Mn₂Au is dragged along by the permalloy, leading to a coupled domain wall motion.

We analyze this coupled domain wall motion for different magnetic field strengths. In Fig. 4(a) we show snapshots of the domain wall profile at different times for various magnetic field strengths. Besides extending the [110] domain, the field rotates the [1-10] domain such that the x component of the magnetic order parameter assumes the shifted value of $n_x = -1/\sqrt{2} + \delta n_x$. In Fig. 4(b) we display $\delta \phi$ [31] as a function of the applied field strength. At the critical field B_c , the domain wall flips to a uniform state, which induces a jump in δn_x . This is in agreement with Sec. III, where we find a magnetic field induced shift $\delta \phi$ in the position of the energy minimum for the domain that is oriented approximately perpendicular to the magnetic field, with $\delta n_x = 1/\sqrt{2} - \cos(\delta \phi - \pi/2)$.

In Fig. 4(c) we show the domain wall velocities as a function of the applied magnetic field strength. As expected, the domain wall moves faster for stronger applied fields. The existence of a critical magnetic field above which the domain wall is flipped into a single domain state, however, puts a boundary on the maximally possible domain wall speed induced by magnetic fields. We fitted our simulation data using Eq. (8) from [32] from which we obtain a velocity of $c \approx 8.5$ km/s.

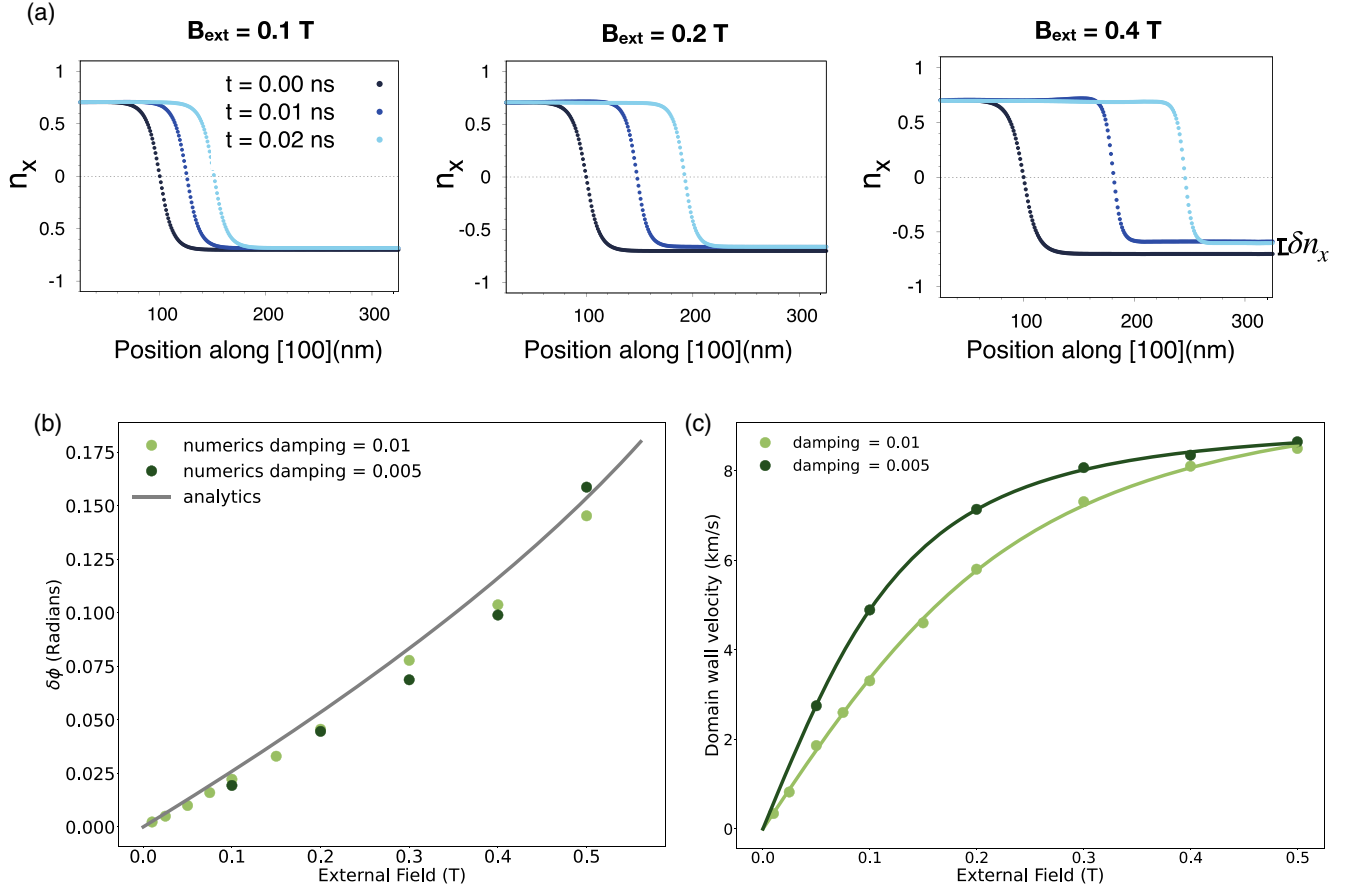


FIG. 4. Magnetic field-driven domain wall motion for a Py thickness of 1 nm. (a) Domain wall profile snapshots for varying field strengths. This is the height-averaged magnetization of one AFM sublattice. (b) Change in domain orientation $\delta\phi$ as a function of magnetic field strength. (c) Domain wall velocity as a function of applied field strength. The simulation data was fitted using Eq. (9) from [32].

In our numerics, the magnetic field-driven domain walls have velocities between 0.1–8.5 km/s with maximum possible values of 8.5 km/s close to B_c . Here we disregard the Oersted field generated by the charge current inside Mn_2Au . In the real experiment, both the effect of the NSOT and the magnetic field will add up.

B. Néel spin-orbit torque driven domain wall dynamics

In the Mn_2Au -Py bilayers, the SOTs are induced by the Au atoms. The Au atoms cause spin-dependent scattering in the Mn_2Au and, due to the spin symmetry around the Au sites, this leads to a Néel SOT acting in opposite directions on the different sublattices. Contrary to SOTs, Néel SOTs are not a surface effect, but act in the bulk. Therefore, the SOTs act only on the Mn atoms and there are no SOTs in the Py capping layer [1–3,33].

To study the domain wall dynamics induced by Néel SOTs, we add the Néel SOT \mathbf{B}_{NSOT} to the effective field in the LLG equation, Eq. (9),

$$\mathbf{B}_{\text{eff}} = -\frac{\delta\mathcal{H}}{\delta\mathbf{S}_i} + \mathbf{B}_{\text{NSOT}}, \quad (10)$$

where

$$\mathbf{B}_{\text{NSOT}} = B_{\text{DT}}^{\text{NSOT}} (\boldsymbol{\sigma} - \lambda \mathbf{S} \times \boldsymbol{\sigma}) + B_{\text{FT}}^{\text{NSOT}} (\mathbf{S} \times \boldsymbol{\sigma} + \lambda \boldsymbol{\sigma}), \quad (11)$$

comprises both the fieldlike ($B_{\text{FT}}^{\text{NSOT}}$) and dampinglike Néel SOTs ($B_{\text{DT}}^{\text{NSOT}}$) [34,35] acting on the Mn_2Au layers. The directions of the SOTs are defined by the spin polarization unit vector $\boldsymbol{\sigma}$. The spin polarization unit vector acts perpendicular to the electron flow. Here the electron flow is along [001], and the SOTs act along [110] and $[-1-10]$ in the two Mn sublattices, respectively, effectively shifting the domain wall along the [100] axis. The Néel SOT field strengths $B_{\text{FT}}^{\text{NSOT}}$ and $B_{\text{DT}}^{\text{NSOT}}$ for an atomistic monolayer are given by [34]

$$B_{\text{FT}}^{\text{NSOT}} = \frac{\hbar j_e \theta_{\text{SH}} a^2}{2e \mu_{\text{Mn}}}, \quad (12a)$$

$$B_{\text{DT}}^{\text{NSOT}} = \beta_{\text{NSOT}} B_{\text{FT}}^{\text{NSOT}}, \quad (12b)$$

where j_e is the injected current density and a is the unit cell size. The spin Hall angle θ_{SH} gives the conversion efficiency of electrical current into spin current. β_{NSOT} is an empirical scaling factor that relates the strength of the precessional term with the relaxation term, here assumed to equal one.

In Fig. 5(a) we show the domain wall profiles at 0.00 ns, 0.01 ns, and 0.02 ns for low to higher spin current strengths; $j_e = 0.049$ MA/cm², 0.098 MA/cm², and 0.196 MA/cm² corresponding to $B_{\text{DT}}^{\text{NSOT}} = 0.01$ T, 0.02 T, and 0.04 T. For higher spin current strengths, the current causes deformations in the shape of the domain wall profile over time. After the

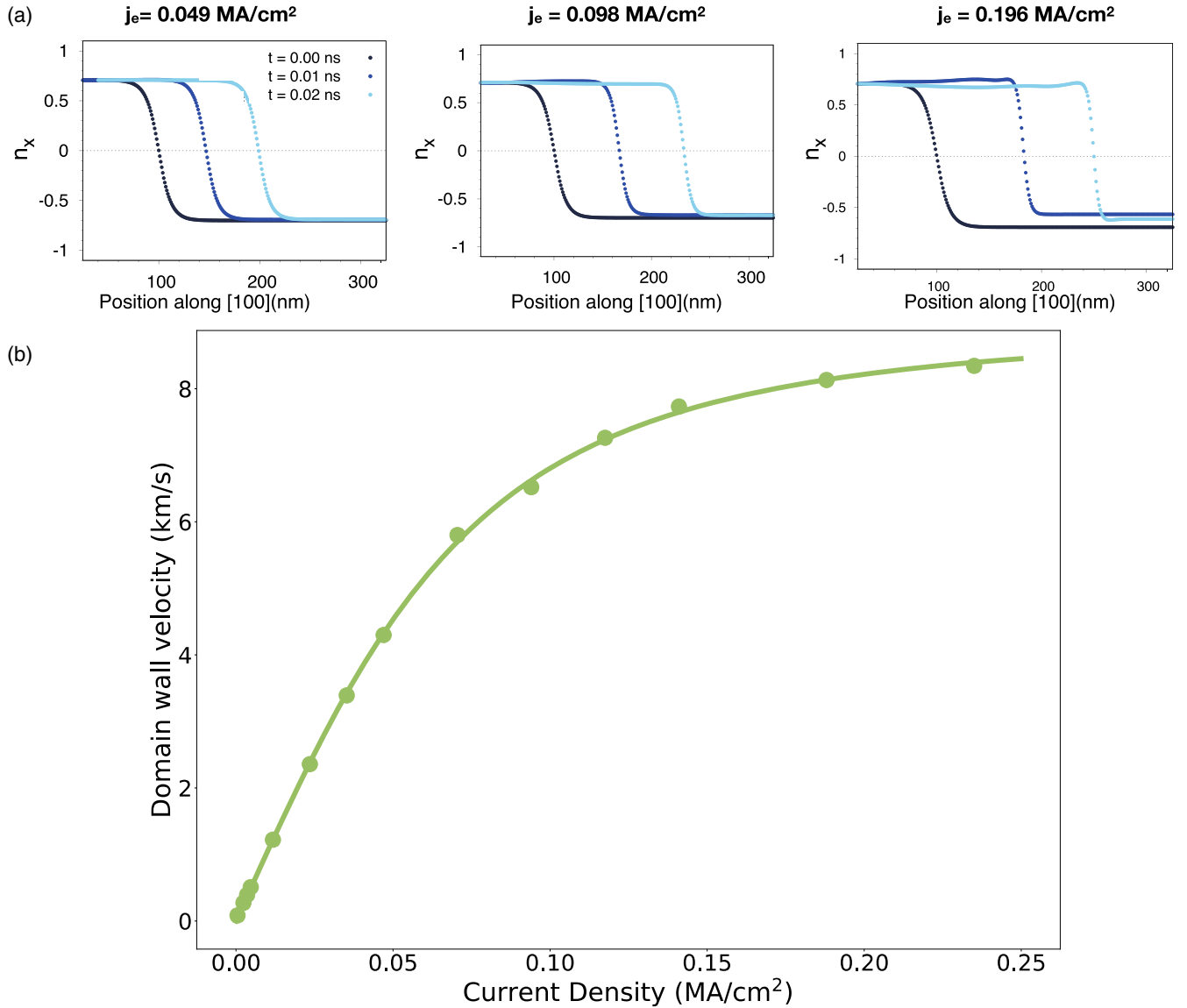


FIG. 5. Current driven domain wall motion for a Py thickness of 1 nm. (a) Domain wall profile snapshots for varying current strengths. This is the height-averaged magnetization of one AFM sublattice. (b) Domain wall velocity as a function of the applied current strength. The simulation data was fitted using Eq. (9) from [32].

initial transient dynamics due to switching on the current, the domain wall reaches a steady state shape and motion in which we compute the domain wall velocity as the average of the gradient of position vs time. We fitted our simulation data using Eq. (8) from [32] from which we obtain a velocity of $c \approx 8.5 \text{ km/s}$. For our chosen parameters we find the maximum velocity of Néel SOT-driven domain walls to be again close to 8.5 km/s even for low currents on the order of 1 MA/cm^2 .

VI. DISCUSSION AND SUMMARY

We have shown that bilayer systems consisting of a thin permalloy capping on top of Mn_2Au display strongly coupled domain wall structures, where the domain wall structure of the AFM is imprinted on the FM. A clear advantage of the thin permalloy capping is that the magnetic dynamics of Mn_2Au

become experimentally observable via the magnetization of the permalloy [19]. Recent experiments have discovered thermally driven short range fluctuations in nanometer spatial ranges in ferromagnets [36]. The influence of thermal effects on our model system has not been studied yet. Furthermore, we have shown that the coupled magnetic textures can be manipulated by two mechanisms: magnetic fields and Néel SOTs. While the applied magnetic field acts mainly in the permalloy, the Néel SOTs act in the Mn_2Au . In both cases, the strong coupling between the layers causes the spin dynamics in one layer to affect the spin dynamics in the other layer which finally induces a collective domain wall motion. Notably the domain wall motion is independent of the driving mechanism and the material it originated from. For both magnetic field and Néel SOT-driven domain walls we obtain velocities on the order of 8.5 km/s . Such a controlled manipulation of the AFM is a key requirement for AFM-based

high-density storage and efficient THz information and computing technologies.

ACKNOWLEDGMENTS

We thank Richard Evans, Ricardo Rama-Eiroa, Rubén M. Otxoa, Roy Chantrell, Martin Jourdan, and Satya Prakash Bommanaboyena for fruitful discussions. We acknowledge funding from the German Research Foundation (DFG) - TRR 173 268565370 Spin+X: spin in its collective environment (project B12 and A05), Project No. 320163632 (Emmy Noether), CRC/TRR 270 - ProjectID 405553726 (Project B12). This project made use of the MagnitUDE cluster, a high-performance computing facility provided by the University of Duisburg-Essen.

S.J. performed the atomistic spin dynamics simulations and the associated data post processing. T.W. provided the phenomenological model. S.J., K.E.S., and T.W. prepared the manuscript. K.E.S. and O.G. provided the scientific leadership of the project and helped with proofreading the manuscript.

APPENDIX A: SIMULATION DETAILS

The parameters used for the atomistic simulations are summarized in Table I and explained in more detail below.

The crystal structure of Mn_2Au with unit cell dimensions a , b , and c is shown in Fig. 6. J_1 , J_2 , and J_3 indicate the isotropic exchange parameters for the nearest neighbor, next nearest neighbor, and next-next nearest neighbor, at distances 2.180 Å, 2.853 Å, and 3.327 Å, respectively.

In the simulations for the isotropic exchange in Mn_2Au , the exchange interactions were taken into account up to the next-next nearest neighbor with parameters from

TABLE I. Model parameters for Mn_2Au used in the simulations. Isotropic exchange parameters are taken from Khmelevskiy *et al.* [37] and magnetic anisotropies are taken from Shick *et al.* [22]. The magnetic moment of the Mn sites is taken from experimental measurements of Barthem *et al.* [26].

Interaction	J_{xx}	J_{yy}	J_{zz}	Unit
$\mathbf{J}_1^{\text{Mn}_2\text{Au}}$	-1.094296	-1.094296	-1.086911	10^{-20} J (per link)
$\mathbf{J}_2^{\text{Mn}_2\text{Au}}$	-1.469234	-1.469234	-1.459319	10^{-20} J (per link)
$\mathbf{J}_3^{\text{Mn}_2\text{Au}}$	0.318261	0.318261	0.318261	10^{-20} J (per link)
$\tilde{\mathbf{J}}_1^{\text{Mn}_2\text{Au}}$	0.0	0.0	0.007385	10^{-20} J (per link)
$\tilde{\mathbf{J}}_2^{\text{Mn}_2\text{Au}}$	0.0	0.0	0.009915	10^{-20} J (per link)
$\tilde{\mathbf{J}}_3^{\text{Mn}_2\text{Au}}$	0.0	0.0	0.318261	10^{-20} J (per link)
$\tilde{\mathbf{J}}^{\text{Py}}$	0.009915	0.009915	0.009915	10^{-20} J (per link)
$\tilde{\mathbf{J}}^{\text{int}}$	0.318261	0.318261	0.318261	10^{-20} J (per link)
Parameter	Value	Unit		
a, b	3.327	Å		
c	8.539	Å		
μ_{Mn}	4.0	μ_{B}		
μ_{Py}	1.6	μ_{B}		
$k_4^{\text{Mn}_2\text{Au}}$	-1.60218×10^{-24}	J/atom		
$k_\phi^{\text{Mn}_2\text{Au}}$	8.00109×10^{-25}	J/atom		
k_c^{Py}	1.0×10^{-26}	J/atom		
$\lambda_{\text{Mn}_2\text{Au}}$	0.01			
λ_{Py}	0.01			

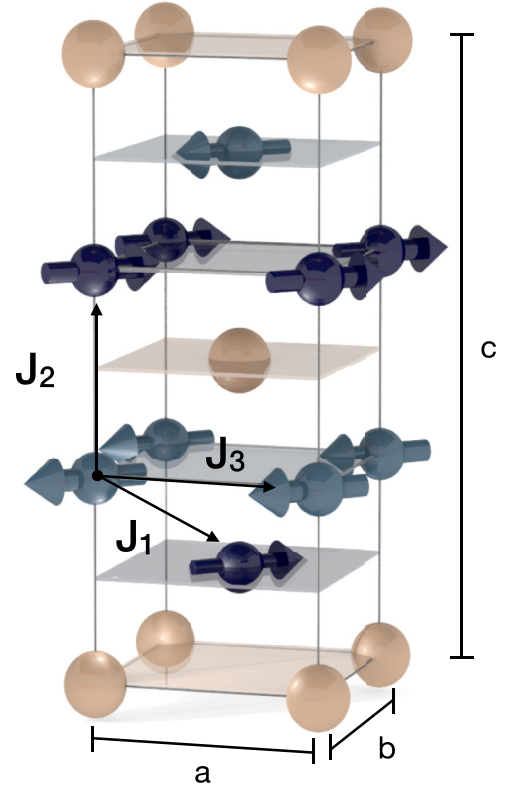


FIG. 6. Crystal structure of Mn_2Au including the nearest, next, and next-next nearest neighbor interactions.

Khmelevskiy *et al.* [37]. The magnetic anisotropies are taken from Shick *et al.* [22] and the magnetic moment of the manganese sites is taken from experimental measurements of Barthem *et al.* [26].

For permalloy, we consider only the nearest neighbor FM interaction and the weak cubic anisotropy with k_c^{Py} taken from Ellis *et al.* [38].

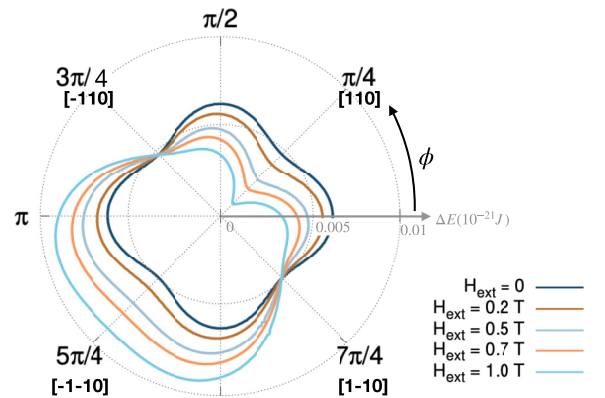


FIG. 7. Spherical plot of energy surfaces of a Mn_2Au -Py bilayer (average energy per atom) with an applied field of varying strength along the [110] direction. Larger radii correspond to larger energies.

For the interface between Mn₂Au and permalloy, we chose an exchange constant of $J^{\text{int}} = 0.31 \cdot 10^{-20}$ J (per link) being roughly 20% of the bulk exchange value of Mn₂Au. This value is motivated by recent experiments where the interface coupling has been found to be strong [19]. For the damping parameters λ_{Py} and $\lambda_{\text{Mn}_2\text{Au}}$ we used 0.01 if not stated otherwise.

APPENDIX B: SINGLE DOMAIN STATES / SPHERICAL VERSION

Figure 7 shows the spherical version of Fig. 2 of the main text. It reveals the transition from the fourfold rotational symmetry in the absence of a magnetic field, to a remaining mirror symmetry in the direction of the magnetic field.

- [1] A. H. MacDonald and M. Tsoi, Antiferromagnetic metal spintronics, *Philos. Trans. R. Soc. London A* **369**, 3098 (2011).
- [2] E. V. Gomonay and V. M. Loktev, Spintronics of antiferromagnetic systems, *Low Temp. Phys.* **40**, 17 (2014).
- [3] T. Jungwirth, X. Marti, P. Wadley, and J. Wunderlich, Antiferromagnetic spintronics, *Nat. Nanotechnol.* **11**, 231 (2016).
- [4] V. Baltz, A. Manchon, M. Tsoi, T. Moriyama, T. Ono, and Y. Tserkovnyak, Antiferromagnetic spintronics, *Rev. Mod. Phys.* **90**, 015005 (2018).
- [5] T. Jungwirth, J. Sinova, A. Manchon, X. Marti, J. Wunderlich, and C. Felser, The multiple directions of antiferromagnetic spintronics, *Nat. Phys.* **14**, 200 (2018).
- [6] M. B. Jungfleisch, W. Zhang, and A. Hoffmann, Perspectives of antiferromagnetic spintronics, *Phys. Lett. A* **382**, 865 (2018).
- [7] S. Fukami, V. O. Lorenz, and O. Gomonay, Antiferromagnetic spintronics, *J. Appl. Phys.* **128**, 070401 (2020).
- [8] P. Wadley, B. Howells, J. Železný, C. Andrews, V. Hills, R. P. Campion, V. Novák, K. Olejník, F. Maccherozzi, S. S. Dhesi, S. Y. Martin, T. Wagner, J. Wunderlich, F. Freimuth, Y. Mokrousov, J. Kuneš, J. S. Chauhan, M. J. Grzybowski, A. W. Rushforth, K. W. Edmonds *et al.*, Electrical switching of an antiferromagnet, *Science* **351**, 587 (2016).
- [9] K. Olejník, V. Schuler, X. Marti, V. Novák, Z. Kašpar, P. Wadley, R. P. Campion, K. W. Edmonds, B. L. Gallagher, J. Garces, M. Baumgartner, P. Gambardella, and T. Jungwirth, Antiferromagnetic CuMnAs multi-level memory cell with microelectronic compatibility, *Nat. Commun.* **8**, 15434 (2017).
- [10] K. Olejník, T. Seifert, Z. Kašpar, V. Novák, P. Wadley, R. P. Campion, M. Baumgartner, P. Gambardella, P. Němec, J. Wunderlich, J. Sinova, P. Kužel, M. Müller, T. Kampfrath, and T. Jungwirth, Terahertz electrical writing speed in an antiferromagnetic memory, *Sci. Adv.* **4**, eaar3566 (2018).
- [11] T. Matalla-Wagner, M.-F. Rath, D. Graulich, J.-M. Schmalhorst, G. Reiss, and M. Meinert, Electrical Néel-order switching in magnetron-sputtered CuMnAs thin films, *Phys. Rev. Appl.* **12**, 064003 (2019).
- [12] M. Meinert, D. Graulich, and T. Matalla-Wagner, Electrical switching of antiferromagnetic Mn₂Au and the role of thermal activation, *Phys. Rev. Appl.* **9**, 064040 (2018).
- [13] Y. Behovits, A. L. Chekhov, S. Y. Bodnar, O. Gueckstock, S. Reimers, Y. Lytvynenko, Y. Skourski, M. Wolf, T. S. Seifert, O. Gomonay, M. Kläui, M. Jourdan, and T. Kampfrath, Terahertz Néel spin-orbit torques drive nonlinear magnon dynamics in antiferromagnetic Mn₂Au, *Nat. Commun.* **14**, 6038 (2023).
- [14] S. Reimers, Y. Lytvynenko, Y. R. Niu, E. Golias, B. Sarpi, L. S. I. Veiga, T. Denneulin, A. Kovács, R. E. Dunin-Borkowski, J. Bläßer, M. Kläui, and M. Jourdan, Current-driven writing process in antiferromagnetic Mn₂Au for memory applications, *Nat. Commun.* **14**, 1861 (2023).
- [15] Y. Cheng, S. Yu, M. Zhu, J. Hwang, and F. Yang, Electrical switching of tristate antiferromagnetic Néel order in α -Fe₂O₃ epitaxial films, *Phys. Rev. Lett.* **124**, 027202 (2020).
- [16] T. Hajiri, S. Ishino, K. Matsuura, and H. Asano, Electrical current switching of the noncollinear antiferromagnet Mn₃GaN, *Appl. Phys. Lett.* **115**, 052403 (2019).
- [17] M. Dunz, T. Matalla-Wagner, and M. Meinert, Spin-orbit torque induced electrical switching of antiferromagnetic MnN, *Phys. Rev. Res.* **2**, 013347 (2020).
- [18] J. Shi, V. Lopez-Dominguez, F. Garesci, C. Wang, H. Almasi, M. Grayson, G. Finocchio, and P. K. Amiri, Electrical manipulation of the magnetic order in antiferromagnetic PtMn pillars, *Nat. Electron.* **3**, 92 (2020).
- [19] S. P. Bommanaboyena, D. Backes, L. S. I. Veiga, S. S. Dhesi, Y. R. Niu, B. Sarpi, T. Denneulin, A. Kovács, T. Mashoff, O. Gomonay, J. Sinova, K. Everschor-Sitte, D. Schönke, R. M. Reeve, M. Kläui, H.-J. Elmers, and M. Jourdan, Readout of an antiferromagnetic spintronics system by strong exchange coupling of Mn₂Au and permalloy, *Nat. Commun.* **12**, 6539 (2021).
- [20] H. Al-Hamdo, T. Wagner, Y. Lytvynenko, G. Kendzo, S. Reimers, M. Ruhwedel, M. Yaqoob, V. I. Vasyuchka, P. Pirro, J. Sinova, M. Kläui, M. Jourdan, O. Gomonay, and M. Weiler, Coupling of ferromagnetic and antiferromagnetic spin dynamics in Mn₂Au/NiFe thin film bilayers, *Phys. Rev. Lett.* **131**, 046701 (2023).
- [21] P. Wadley, K. W. Edmonds, M. R. Shahedkhah, R. P. Campion, B. L. Gallagher, J. Železný, J. Kuneš, V. Novák, T. Jungwirth, V. Saitl, P. Němec, F. Maccherozzi, and S. S. Dhesi, Control of antiferromagnetic spin axis orientation in bilayer Fe/CuMnAs films, *Sci. Rep.* **7**, 11147 (2017).
- [22] A. B. Shick, S. Khmelevskiy, O. N. Mryasov, J. Wunderlich, and T. Jungwirth, Spin-orbit coupling induced anisotropy effects in bimetallic antiferromagnets: A route towards antiferromagnetic spintronics, *Phys. Rev. B* **81**, 212409 (2010).
- [23] R. F. L. Evans, L. Rózsa, S. Jenkins, and U. Atxitia, Temperature scaling of two-ion anisotropy in pure and mixed anisotropy systems, *Phys. Rev. B* **102**, 020412 (2020).
- [24] R. F. L. Evans, W. J. Fan, P. Churemart, T. A. Ostler, M. O. A. Ellis, and R. W. Chantrell, Atomistic spin model simulations of magnetic nanomaterials, *J. Phys.: Condens. Matter* **26**, 103202 (2014).
- [25] D. Meilak, S. Jenkins, R. Pond, and R. F. L. Evans, Massively parallel atomistic simulation of ultrafast thermal spin dynamics of a permalloy vortex, [arXiv:1908.08885](https://arxiv.org/abs/1908.08885).
- [26] V. Barthem, C. Colin, H. Mayaffre, M.-H. Julien, and D. Givord, Revealing the properties of Mn₂Au for antiferromagnetic spintronics, *Nat. Commun.* **4**, 2892 (2013).

- [27] J. Hirst, U. Atxitia, S. Ruta, J. Jackson, L. Petit, and T. Ostler, Temperature-dependent micromagnetic model of the antiferromagnet Mn_2Au : A multiscale approach, *Phys. Rev. B* **106**, 094402 (2022).
- [28] P. Asselin, R. F. L. Evans, J. Barker, R. W. Chantrell, R. Yanes, O. Chubykalo-Fesenko, D. Hinzke, and U. Nowak, Constrained Monte Carlo method and calculation of the temperature dependence of magnetic anisotropy, *Phys. Rev. B* **82**, 054415 (2010).
- [29] We constrained the direction of the magnetisation of a single Mn sublattice while allowing all other spins to relax to their equilibrium spin structures.
- [30] J. L. Garcia-Palacios and F. J. Lazaro, Langevin-dynamics study of the dynamical properties of small magnetic particles, *Phys. Rev. B* **58**, 14937 (1998).
- [31] In Mn_2Au , the achieved DW velocity v is much lower than c , i.e. $vc \ll 1$. Therefore canting between the magnetic sublattices can be neglected. The limiting DW velocity is determined by the critical switching field. For the calculation of the DW velocity the full spin texture is used.
- [32] O. Gomonay, T. Jungwirth, and J. Sinova, High antiferromagnetic domain wall velocity induced by Néel spin-orbit torques, *Phys. Rev. Lett.* **117**, 017202 (2016).
- [33] J. Železný, H. Gao, K. Výborný, J. Zemen, J. Mašek, A. Manchon, J. Wunderlich, J. Sinova, and T. Jungwirth, Relativistic Néel-order fields induced by electrical current in antiferromagnets, *Phys. Rev. Lett.* **113**, 157201 (2014).
- [34] A. Manchon, J. Železný, I. M. Miron, T. Jungwirth, J. Sinova, A. Thiaville, K. Garello, and P. Gambardella, Current-induced spin-orbit torques in ferromagnetic and antiferromagnetic systems, *Rev. Mod. Phys.* **91**, 035004 (2019).
- [35] A. Meo, C. E. Cronshaw, S. Jenkins, A. Lees, and R. F. L. Evans, Spin-transfer and spin-orbit torques in the Landau–Lifshitz–Gilbert equation, *J. Phys.: Condens. Matter* **35**, 025801 (2023).
- [36] S. M. Sutorin, A. Philippi-Kobs, R. Carley, R. Gort, G. Grübel, E. Jal, M. V. Baidakova, E. Y. Lobanova, L. Mercadier, S. L. Molodtsov, L. Müller, D. V. Potorochin, M. Riepp, W. Roseker, A. Scherz, J. Schlappa, L. Le Guyader, G. Mercurio, M. Turcato, B. Van Kuiken *et al.*, Short nanometer range optically induced magnetic fluctuations accompanying ultrafast demagnetization of nanoscale ferromagnetic domains, *Phys. Rev. B* **108**, 174444 (2023).
- [37] S. Khmelevskiy and P. Mohn, Layered antiferromagnetism with high Néel temperature in the intermetallic compound Mn_2Au , *Appl. Phys. Lett.* **93**, 162503 (2008).
- [38] M. O. A. Ellis, T. A. Ostler, and R. W. Chantrell, Classical spin model of the relaxation dynamics of rare-earth doped permalloy, *Phys. Rev. B* **86**, 174418 (2012).